Multidimensional encoding of restricted and anisotropic diffusion by double rotation of the *q*-vector

Hong Jiang[1], Leo Svenningsson[1], Daniel Topgaard[1]

[1]Physical Chemistry, Lund University, P.O. Box 124, SE-22100 Lund, Sweden

5 *Correspondence to*: Daniel Topgaard (daniel.topgaard@fkem1.lu.se)

Abstract. Diffusion NMR and MRI methods building on the classic pulsed gradient spin echo sequence are sensitive to many aspects of translational motion, including time/frequency-dependence ("restriction"), anisotropy, and flow, which leads to ambiguities when interpreting experimental data from complex heterogeneous materials such as living biological tissues. Higher specificity to restriction or anisotropy can be obtained with, respectively, oscillating gradient or tensor-valued encoding

10 which nevertheless both have some sensitivity to the property not being of direct interest. Here we propose a simple scheme derived from the "double rotation" technique in solid-state NMR to generate a family of modulated gradient waveforms allowing for comprehensive exploration of the two-dimensional frequency-anisotropy space and convenient investigation of both restricted and anisotropic diffusion with a single multidimensional acquisition protocol. The method is demonstrated by measuring multicomponent isotropic Gaussian diffusion in simple liquids, anisotropic Gaussian diffusion in a polydomain

15 lyotropic liquid crystal, and restricted diffusion in a yeast cell sediment.

1   Introduction

Magnetic field gradients applied during the dephasing and rephasing periods of a spin echo sequence (Hahn, 1950) render the NMR signal sensitive to various aspects of translational motion including bulk diffusivity (Douglass and McCall, 1958), flow (Carr and Purcell, 1954), time/frequency-dependence ("restriction") (Woessner, 1963), anisotropy (Boss and Stejskal, 1965),

20 and exchange (Kärger, 1969). Although the conventional and ubiquitous pulsed gradient spin echo sequence by Stejskal and Tanner (1965) may give information about all of these aspects, more elaborate gradient modulations (Tanner, 1979; Cory et al., 1990; Callaghan and Manz, 1994; Mori and van Zijl, 1995) are required to unambiguously assign a certain mechanism to the experimental observations (Topgaard, 2017; Lundell and Lasič, 2020). Diffusion MRI methods incorporating such advanced diffusion encoding schemes have recently been shown to have potential for clinical research applications (Reymbaut

25 et al., 2020)—some notable examples being oscillating gradients to estimate cell sizes (Xu et al., 2021) and tensor-valued encoding to characterize cell shapes (Daimiel Naranjo et al., 2021) in breast tumors.

The sensitivity of the MRI signal to the various types of motion can be quantified with the tensor-valued encoding spectrum $\mathbf{b}(\omega)$ (Topgaard, 2019b; Lundell and Lasič, 2020), the trace of which equals the dephasing power spectrum (Stepišnik, 1981)—relevant for isotropic restricted diffusion—and whose integral over ω equals the conventional *b*-matrix

30 (Basser et al., 1994) giving information about diffusion anisotropy. While most studies focus on either the frequency-dependent (Aggarwal, 2020) or tensorial (Reymbaut, 2020) aspects of the encoding, Lundell et al. (2019) suggested joining them into a common multidimensional framework. The approach was demonstrated with gradient waveforms deriving from the magic-angle spinning (MAS) technique in solid-state NMR spectroscopy (Andrew et al., 1959; Eriksson et al., 2013; Topgaard, 2013), which, however, offer only limited access to the frequency and anisotropy dimensions.

35 Expanding on the results of Lundell et al. (2019), we here take inspiration from the "double rotation" (DOR) technique in solid-state NMR (Samoson et al., 1998) and derive a family of gradient waveforms for comprehensive exploration of, in particular, the frequency-anisotropy dimensions of $\mathbf{b}(\omega)$, as quantified by the centroid frequency ω_{cent} (Arbabi et al., 2020) and encoding anisotropy b_Δ (Eriksson et al., 2015), in addition to the *b*-value and *b*-vector (Θ,Φ) of conventional diffusion tensor imaging (Kingsley, 2006). While ω_{cent} is key for characterizing restricted diffusion (Stepišnik and Callaghan, 2000), the

40 variable b_Δ enables quantification of anisotropy in orientationally disordered materials (Eriksson et al., 2015) and estimation

1

MAGNETIC RESONANCE
Open Access Discussions

of nonparametric diffusion tensor distributions (de Almeida Martins and Topgaard, 2016; Topgaard, 2019a). The ability of the new gradient waveforms to give access to the complete 2D ω_{cent}-b_Δ plane is demonstrated by microimaging measurements on previously studied phantoms with well-defined restriction and anisotropy properties, namely water (Mills, 1973) and concentrated salt solution (Wadsö et al., 2009) with isotropic Gaussian diffusion, a lamellar liquid crystal giving anisotropic Gaussian diffusion (Topgaard, 2016), and a yeast cell sediment exhibiting isotropic restricted diffusion (Malmborg et al., 2006).

2   Theory

The textbooks by Price (2009) and Callaghan (2011), as well as the comprehensive review by Lundell and Lasič (2020), give detailed accounts of the theory behind diffusion NMR and MRI. For the purpose of this paper, it is sufficient to focus on the Gaussian phase distribution approximation (Stepišnik, 1981, 1993) where the tensor-valued diffusion spectrum $\mathbf{D}(\omega)$ is encoded into the signal attenuation S/S_0 via

$$S/S_0 = \exp\left(-\int_{-\infty}^{\infty} \mathbf{b}(\omega) : \mathbf{D}(\omega)\mathrm{d}\omega\right), \tag{1}$$

where ":" denotes a generalized scalar product (Kingsley, 2006) and $\mathbf{b}(\omega)$ is the tensor-valued encoding spectrum (Topgaard, 2019b; Lundell and Lasič, 2020) given by the time-dependent gradient vector $\mathbf{g}(t)$, time-dependent dephasing vector $\mathbf{q}(t)$, and spectrum of the dephasing vector $\mathbf{q}(\omega)$ through

$$\mathbf{q}(t) = \gamma \int_0^t \mathbf{g}(t')\mathrm{d}t', \tag{2}$$

$$\mathbf{q}(\omega) = \int_0^\tau \mathbf{q}(t)\exp(\mathrm{i}\omega t)\,\mathrm{d}t, \tag{3}$$

and

$$\mathbf{b}(\omega) = \frac{1}{2\pi}\mathbf{q}(\omega)\mathbf{q}(-\omega)^{\mathrm{T}}. \tag{4}$$

At each frequency ω, both $\mathbf{b}(\omega)$ and $\mathbf{D}(\omega)$ are symmetric second-order tensors. The conventional dephasing power spectrum $b(\omega)$ (Stepišnik, 1981) and b-matrix $\mathbf{b}$ (Basser et al., 1994) are obtained from $\mathbf{b}(\omega)$ by

$$b(\omega) = \text{trace}\{\mathbf{b}(\omega)\} \tag{5}$$

and

$$\mathbf{b} = \int_{-\infty}^{\infty} \mathbf{b}(\omega)\mathrm{d}\omega. \tag{6}$$

The sensitivity to restriction and anisotropy may be summarized by the centroid frequency ω_{cent} (Arbabi et al., 2020) and encoding anisotropy b_Δ (Eriksson et al., 2015) given by

$$\omega_{\text{cent}} = \frac{1}{b}\int_{-\infty}^{\infty}|\omega|b(\omega)\mathrm{d}\omega \tag{7}$$

and

$$b_\Delta = \frac{1}{b}\left(b_{ZZ} - \frac{b_{YY} + b_{XX}}{2}\right), \tag{8}$$

where

$$b = \text{trace}\{\mathbf{b}\} \tag{9}$$

is the conventional b-value (Le Bihan et al., 1986) and b_{XX}, b_{YY}, and b_{ZZ} are the eigenvalues of $\mathbf{b}$ ordered according to the Haeberlen convention $|b_{ZZ} - b/3| > |b_{XX} - b/3| > |b_{YY} - b/3|$ (Haeberlen, 1976). Additionally, the encoding asymmetry b_η is defined by (Eriksson et al., 2015)

$$b_\eta = \frac{3}{2} \frac{b_{YY} - b_{XX}}{b b_\Delta}. \tag{10}$$

For the special cases of (i) isotropic Gaussian, (ii) anisotropic Gaussian, and (iii) isotropic restricted diffusion, the signal expression in Eq (1) can be rewritten as

$$S/S_0 = \exp(-bD), \tag{11}$$

$$S/S_0 = \exp(-\mathbf{b}\!:\!\mathbf{D}), \tag{12}$$

and

$$S/S_0 = \exp\left(-\int_{-\infty}^{\infty} b(\omega) D(\omega)\,\mathrm{d}\omega\right), \tag{13}$$

respectively, where D is the (isotropic and ω-independent) diffusion coefficient, $\mathbf{D}$ the (ω-independent) diffusion tensor, and $D(\omega)$ the (isotropic) diffusion spectrum which all have been extensively used in the diffusion MRI literature.

Assuming axial symmetry of both $\mathbf{b}$ and $\mathbf{D}$, powder averaging of Eq. (12) yields (Eriksson et al., 2015)

$$S/S_0 = \exp(-b D_{\mathrm{iso}}) \frac{\sqrt{\pi}}{2} \frac{\exp(A/3)}{\sqrt{A}} \mathrm{erf}\left(\sqrt{A}\right) \tag{14}$$

where

$$A = 3 b D_{\mathrm{iso}} b_\Delta D_\Delta. \tag{15}$$

In Eq. (15), D_{iso} is the isotropic diffusivity and D_Δ the normalized diffusion anisotropy defined as

$$D_{\mathrm{iso}} = \frac{1}{3} \text{trace}\{\mathbf{D}\} \tag{16}$$

and

$$D_\Delta = \frac{D_{\mathrm{A}} + D_{\mathrm{R}}}{3 D_{\mathrm{iso}}}, \tag{17}$$

where D_{A} and D_{R} are the axial radial eigenvalues of $\mathbf{D}$. Eq. (14) is used to fit the liquid crystal data in Figure 3(b).

For restricted diffusion of a liquid with bulk diffusivity D_0 in a sphere with radius r, the diffusion spectrum $D(\omega)$ is given by (Stepišnik, 1993)

$$D(\omega) = D_0 \left(1 - \sum_k w_k \frac{1}{1 + \omega^2/\Gamma_k^2}\right) \tag{18}$$

where

$$w_k = \frac{2}{\alpha_k^2 - 2} \tag{19}$$

and

$$\Gamma_k = \frac{\alpha_k^2 D_0}{r^2}. \tag{20}$$

In Eq. (20), α_k is the kth solution of

$$\alpha J_{1/2}(\alpha) - 2J_{3/2}(\alpha) = 0, \tag{21}$$

where J_v is the vth order Bessel function of the first kind. Eq. (13) with Eq. (18) is used to fit the yeast data in Figure 3(c).

3 Design of gradient waveforms by double rotation of the q-vector

85 Expanding on previous magic-angle spinning (Andrew et al., 1959; Eriksson et al., 2013; Topgaard, 2013) and variable-angle spinning (Frydman et al., 1992; Topgaard, 2016, 2017) approaches for generating motion-encoding gradient waveforms, we here apply the double rotation (DOR) technique (Samoson et al., 1998; Topgaard, 2019b) to probe the 2D acquisition space spanned by the variables ω_{cent} and b_Δ. Following previous works (Eriksson et al., 2013), the q-vector trajectory $\mathbf{q}(t)$ is expressed in terms of its time-dependent magnitude $q(t)$ and unit vector $\mathbf{u}(t)$ as

$$\mathbf{q}(t) = q(t)\mathbf{u}(t). \tag{22}$$

90 For the special case of DOR, the unit vector is written as

$$\mathbf{u}(t) = \mathbf{R}_z\big(\psi_2(t)\big)\mathbf{R}_y(\zeta_2)\mathbf{R}_z\big(\psi_1(t)\big)\mathbf{R}_y(\zeta_1)[0 \quad 0 \quad 1]^T, \tag{23}$$

where $\mathbf{R}_z$ and $\mathbf{R}_y$ are Euler rotation matrices, ζ_1 and ζ_2 are the inclinations of the two rotation axes, and $\psi_1(t)$ and $\psi_2(t)$ are the time-dependent angles of rotation. The rotations in Eq. (23) are applied from right to left and follow a Z-Y active rotation matrix convention.

Starting from a conventional one-dimensional gradient waveform $g_{1D}(t)$–for instance a pair of rectangular or sine-bell
95 pulses of opposite polarity–the time-dependent functions $q(t)$ and $\psi_2(t)$ are given by (Topgaard, 2016)

$$q(t) = \gamma \int_0^t g_{1D}(t')\mathrm{d}t' \tag{24}$$

and

$$\psi_2(t) = \frac{\Delta\psi_2}{b} \int_0^t q^2(t')\mathrm{d}t', \tag{25}$$

where $\Delta\psi_2$ is the total angle of rotation during the encoding interval from time $t = 0$ to τ and

$$b = \int_0^\tau q^2(t)\mathrm{d}t \tag{26}$$

is the conventional b-value. After some exercises in trigonometry, combination of Eqs. (22)-(26) and the relation between $\mathbf{g}(t)$ and $\mathbf{q}(t)$ in Eq.(2) yields

$$
\begin{aligned}
\mathbf{g}_{DOR}(t) = g_{1D}(t) &\begin{pmatrix} a_+ \cos\psi_+(t) + a_- \cos\psi_-(t) + a_2 \cos\psi_2(t) \\ a_+ \sin\psi_+(t) - a_- \sin\psi_-(t) + a_2 \sin\psi_2(t) \\ a_0 - a_1 \cos\psi_1(t) \end{pmatrix} \\
+ g_{rot}(t) &\begin{pmatrix} -(n+1)a_+ \sin\psi_+(t) - (n-1)a_- \sin\psi_-(t) - a_2\sin\psi_2(t) \\ (n+1)a_+ \cos\psi_+(t) - (n-1)a_- \cos\psi_-(t) + a_2 \cos\psi_2(t) \\ na_1 \sin\psi_1(t) \end{pmatrix},
\end{aligned}
\tag{27}
$$

100 where

MAGNETIC RESONANCE
Open Access Discussions

$$g_{\text{rot}}(t) = \frac{\Delta\psi_2 q(t)^3}{\gamma b} \tag{28}$$

is the time-dependent magnitude of the rotating gradient vector,

$$\psi_1(t) = n\psi_2(t)$$
$$\psi_\pm(t) = (n \pm 1)\psi_2(t) \tag{29}$$

are time-dependent rotation angles, and

$$a_0 = \cos\zeta_1 \cos\zeta_2$$
$$a_1 = \sin\zeta_1 \sin\zeta_2$$
$$a_2 = \cos\zeta_1 \sin\zeta_2$$
$$a_\pm = \sin\zeta_1 \frac{\cos\zeta_2 \pm 1}{2} \tag{30}$$

are amplitudes of the oscillating terms. At the selected inclinations $\zeta_1 = \pi/2$ and $\zeta_2 = -a\cos(1/3^{1/2})$, the a_0 and a_2 terms in Eq. (27) vanish while the remaining amplitudes evaluate to $a_1 = -(2/3)^{1/2} \approx -0.816$, $a_+ = (3^{-1/2} + 1)/2 \approx 0.789$, and $a_- = (3^{-1/2} - 1)/2 \approx -0.211$. For $n > 1$ and the special case of $g_{1D}(t) \propto [\delta(t) - \delta(t - \tau)]$, where $\delta(x)$ is the Dirac delta function, these inclinations yield an isotropic b-tensor, corresponding to $b_\Delta = 0$. Waveforms for any values of b_Δ and b_η are then conveniently obtained by scaling the components of $\mathbf{g}_{\text{DOR}}(t)$ according to

$$\mathbf{g}(t) = \begin{bmatrix} g_X(t) \\ g_Y(t) \\ g_Z(t) \end{bmatrix} = \begin{bmatrix} g_{\text{DOR},X}(t)\sqrt{1 - b_\Delta(1 + b_\eta)} \\ g_{\text{DOR},Y}(t)\sqrt{1 - b_\Delta(1 - b_\eta)} \\ g_{\text{DOR},Z}(t)\sqrt{1 + 2b_\Delta} \end{bmatrix}. \tag{31}$$

For the special case $g_{1D}(t) \propto [\delta(t) - \delta(t - \tau)]$, the main frequency components of $\mathbf{b}(\omega)$ are given by

$$\omega_\pm = \frac{\psi_\pm(\tau)}{\tau} = (n \pm 1)\frac{\Delta\psi_2}{\tau} \quad \text{and}$$
$$\omega_1 = \frac{\psi_1(\tau)}{\tau} = n\frac{\Delta\psi_2}{\tau}, \tag{32}$$

where, according to Eq. (27), $\omega_\pm$ and ω_1 are cleanly separated into the X,Y and Z directions, respectively. The mean frequency content, as quantified by the centroid frequency ω_{cent} defined in Eq. (7), can be estimated by weighting the contributions from the main frequency components with the corresponding amplitudes Eq. (27), but is more accurately calculated by numerical evaluation of Eq. (7) which also takes the finite durations of the sinusoidal oscillations into account. For rough prediction of ω_{cent} it is useful to note that $a_+^2 >> a_-^2$, implying that the ω_+-component will dominate the spectra in the X,Y-directions. The scaling of the waveforms according to Eq. (31) preserves the frequency content in each of the eigendirections of the b-tensor, but shifts the value of ω_{cent} between the approximate extremes ω_+ and ω_1 for $b_\Delta = -1/2$ and 1, respectively.

Figure 1 illustrates the series of calculations required to convert a conventional 1D waveform $g_{1D}(t)$ and given values of ζ_1, ζ_2, $\Delta\psi_2$, n, b_Δ, and b_η to a 3D waveform $\mathbf{g}(t)$ by numerical evaluation of Eqs. (24)-(31). Following previous works to generate families of smooth gradient waveforms to explore the b_Δ and b_η dimensions of diffusion encoding (Topgaard, 2016, 2017), we here construct $g_{1D}(t)$ from a dephasing lobe with quarter-sine ramp up of duration ε_{up} and half-cosine ramp down of duration $\varepsilon_{\text{down}}$, as well as a rephasing lobe obtained by inversion and time-reversal of the dephasing one. The corresponding Matlab code is provided in the supporting information.
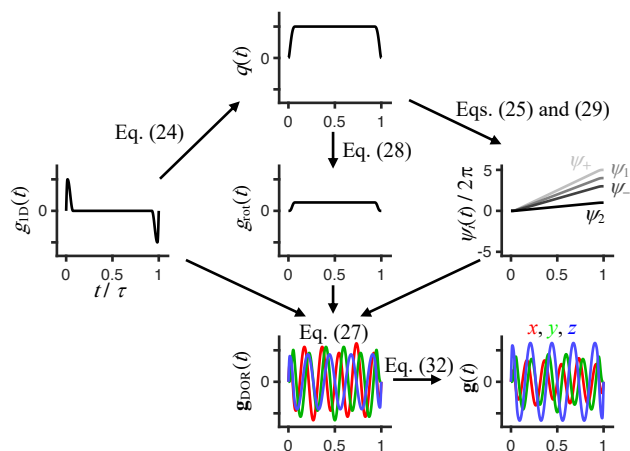
Figure 1. Flow chart for calculating a double-rotation gradient waveform $\mathbf{g}_{DOR}(t)$ given a one-dimensional dephasing/rephasing waveform $g_{1D}(t)$, rotation axis inclinations ζ_1 and ζ_2, double rotation ratio n, and total angle of rotation $\Delta\psi_2$ during the waveform duration τ. The waveform $g_{1D}(t)$, containing dephasing and rephasing pulses with sinusoidal ramps of durations ε_{up} and ε_{down}, gives the time-dependent magnitude of the dephasing vector $q(t)$ by Eq. (24), which yields the time-dependent rotation angles $\psi_i(t)$ via Eqs. (25) and (29) as well as the time-dependent magnitude of the rotating/oscillating gradient $g_{rot}(t)$ through Eq. (28). Combining $g_{1D}(t)$, $g_{rot}(t)$, and $\psi_i(t)$ via Eq. (27) gives $\mathbf{g}_{DOR}(t)$, which if $\zeta_1 = \pi/2$, $\zeta_2 = -\mathrm{acos}(1/3^{1/2})$, n is an integer above 1, and $\Delta\psi_2$ is a multiple of 2π achieves isotropic encoding tensors $\mathbf{b}$ where the anisotropy b_Δ and asymmetry b_η are both equal to zero. Finally, waveforms $\mathbf{g}(t)$ for any values of b_Δ and b_η are obtained by scaling of the Cartesian components of $\mathbf{g}_{DOR}(t)$ according to Eq. (31). The shown example was generated with the accompanying Matlab code (see supporting information) using $\varepsilon_{up} = 0.015\,\tau$, $\varepsilon_{down} = 0.06\,\tau$, $\Delta\psi_2 = 2\pi$, $n = 4$, $b_\Delta = 0.5$, and $b_\eta = 0.25$.

Figure 2 compiles waveforms and encoding spectra for an array of n and b_Δ at constant $g_{1D}(t)$, τ, and $\Delta\psi_2$, yielding constant b. Increasing n leads to larger rotation angles $\psi_1(t)$ and $\psi_\pm(t)$ and frequencies ω_1 and $\omega_\pm$ according to Eqs. (29) and (32), respectively, at the expense of overall higher gradient amplitudes on account of the terms including n in Eq. (27). Many of the waveforms in Figure 2 are familiar from the literature, for instance conventional Stejskal-Tanner encoding at ($n = 0$, $b_\Delta = 1$), basic flow-compensated encoding (Caprihan and Fukushima, 1990) at ($n = 1$, $b_\Delta = 1$), and magic-angle spinning of the q-vector (Eriksson et al., 2013) at ($n = 0$, $b_\Delta = 0$). The series of $b_\Delta = 1$ and $-1/2$ waveforms with varying n resemble, respectively, the cosine-modulated oscillating gradients of Parsons et al. (2003) and the circularly polarized version introduced by Lundell et al. (2015). Correspondingly, the series of waveforms with $n = 0$ and varying b_Δ has previously been introduced as a diffusion version of the variable-angle spinning technique to correlate isotropic and anisotropic chemical shifts in solid-state NMR (Topgaard, 2016, 2017). The approach for joint investigation of restricted and anisotropic diffusion proposed by Lundell et al. (2019), combining isotropic encoding with "tuned" and "detuned" directional encodings, can be recognized as measurements at the three discrete points ($n = 0$, $b_\Delta = 0$), ($n = 0$, $b_\Delta = 1$), and ($n = 1$, $b_\Delta = 1$) of the 2D plane in Figure 2. For completeness, we note that the elliptically polarized oscillating gradients by Nielsen et al. (2018) can be reproduced with $b_\Delta = -1/2$ and b_η in the range from 0 to 3 (not included in Figure 2).
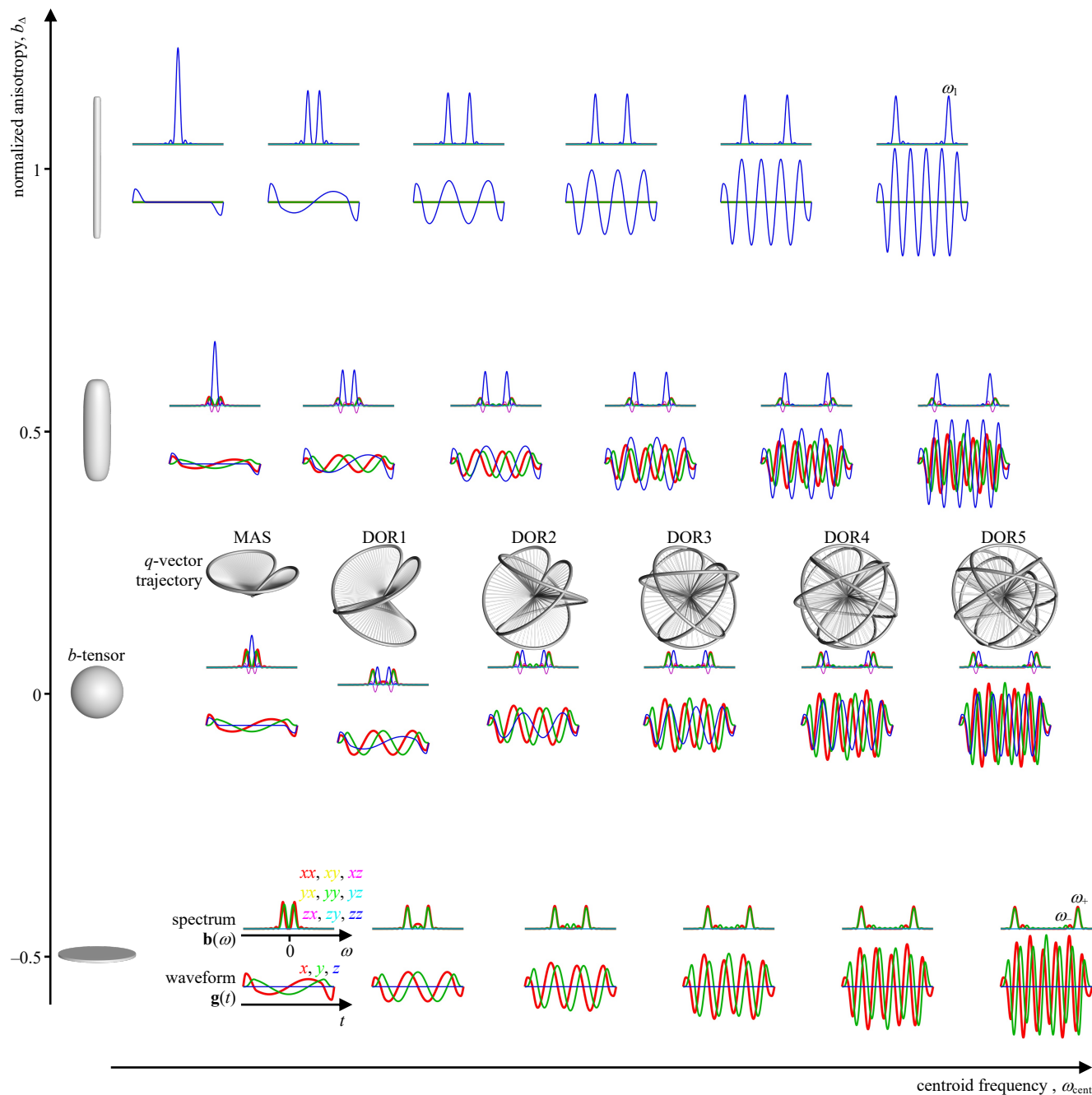
Figure 2. Gradient waveforms $\mathbf{g}(t)$ for comprehensive exploration of the 2D space of centroid frequency ω_{cent} and anisotropy b_Δ of the tensor-valued encoding spectrum $\mathbf{b}(\omega)$. The three-dimensional paths with radial spokes shown for the $b_\Delta = 0$ cases illustrate q-vector trajectories derived from magic-angle spinning (MAS) and double rotation (DORn) with variable frequency ratio n. The waveforms are generated according to the scheme in Figure 1 using $\varepsilon_{\text{up}} = 0.03\,\tau$, $\varepsilon_{\text{down}} = 0.12\,\tau$, $\Delta\psi_2 = 2\pi$, $b_\eta = 0$, and identical b-values for a 2D array of n = 0, 1, ..., 5 and $b_\Delta = -0.5$, 0, 0.5, and 1 with the angles $\zeta_1 = 0$ and $\zeta_2 = \text{acos}(1/3^{1/2})$ for $n = 0$ and $\zeta_1 = \pi/2$ and $\zeta_2 = -\text{acos}(1/3^{1/2})$ for $n > 0$. Superquadric tensor glyphs (Kindlmann, 2004) along the vertical axis indicate the chosen values b_Δ. The main maxima in $\mathbf{b}(\omega)$ are located at the frequencies ω_1 and ω_+ given in Eq. (32). Values of ω_{cent} and b_Δ, including non-idealities originating from the finite durations of the dephasing and rephasing lobes of $g_{1D}(t)$, are obtained by Eqs. (7) and (8) using numerically evaluated $\mathbf{b}(\omega)$ according to Eqs. (2)-(4).

MAGNETIC RESONANCE
Open Access Discussions

155 4   Proof-of-principle experiments

Magnesium nitrate hexahydrate, cobalt nitrate hexahydrate, and 1-decanol were purchased from Sigma-Aldrich Sweden AB and sodium octanoate from J&K Scientific via Th.Geyer in Sweden. Water was purified with a Milli-Q system. A sample with two-component isotropic diffusion was prepared by inserting a 4 mm NMR tube containing an aqueous solution saturated with magnesium nitrate (Wadsö et al., 2009) into a 10 mm NMR tube with water (Mills, 1973). The magnesium nitrate solution

160 was spiked with a small amount cobalt nitrate (0.27 wt% saturated solution) to reduce T_2 to approx. 100 ms. An anisotropic sample was prepared by mixing 85.79 wt% Milli-Q, 9.17 wt% 1-decanol, and 5.04 wt% sodium octanoate giving a lamellar liquid crystal (Persson et al., 1975). Investigation of isotropic non-Gaussian diffusion was performed with a sediment of fresh baker's yeast (trade name: Kronjäst from a local supermarket) prepared by dispersing yeast in tap water (1:1 weight ratio) in a glass vial, transferring with a syringe to a 10 mm NMR tube, and allowing for cell sedimentation overnight at 4 ºC (Malmborg

165 et al., 2006).

MRI was performed on a Bruker Avance-Neo 500 MHz spectrometer equipped with an 11.7 T magnet and a MIC-5 microimaging probe fitted with a 10 mm RF insert for observation of ^{1}H. Images were acquired with a Topspin 4.0 implementation of a spin-echo prepared single-shot RARE sequence (available at https://github.com/daniel-topgaard/md-dmri) using 0.6×0.6 mm^2 in-plane spatial resolution, 1 mm slice thickness, and 16×16×1 matrix size. Diffusion encoding employed

170 pairs of identical gradient waveforms bracketing the 180º pulse in the preparation block (Lasič et al., 2014). Data was acquired for 8 b-values up to 6.44·10^9 sm^{-2} and 15 orientations (Θ,Φ) for each of the 24 waveforms spanning the $\omega_\text{cent},b_\Delta$-plane in Figure 2 using maximum gradient amplitude 3 T/m and waveform duration $\tau = 25$ ms, giving values of ω_cent in the range from 20 to 260 Hz. With 5 s recycle delay, the total measurement time was approximately 4 h for each sample. The sample temperature was controlled with a Bruker VT unit to 278 K for the yeast and 291 K for the isotropic solutions and liquid crystal. Image

175 reconstruction, definition of regions-of-interest, and curve fitting was performed in Matlab using in-house code available at https://github.com/daniel-topgaard/md-dmri (Nilsson et al., 2018).

Figure 3 compiles experimental data and fits for all investigated samples. To facilitate visual inspection of the highly multidimensional data acquired as a function of ($b,\omega_\text{cent},b_\Delta,\Theta,\Phi$), the signal data was averaged over gradient orientations (Θ,Φ) and displayed as conventional Stejskal-Tanner plots of log$_{10}$(signal)-vs.-b with the $\omega_\text{cent},b_\Delta$-dimensions coded into marker

180 grayscale and style. For the isotropic Gaussian sample in Figure 3(a), all data points collapse onto a single master curve, thereby verifying that all 24 waveforms spanning the $\omega_\text{cent},b_\Delta$-plane in Figure 2 indeed give the same b-value. The pronounced non-linearity of the log$_{10}$(signal)-vs.-b plot indicates the presence of multiple species with different diffusivities, and the bi-exponential fit yields values consistent with pure water (fast) and water in the saturated magnesium nitrate solution (slow). The anisotropic Gaussian phantom Figure 3(b) yields data points stratified into one master curve for each of the four values of

185 b_Δ, verifying independence of ω_cent. The data is well fitted by the expression for randomly oriented axisymmetric diffusion tensors in Eq. (14), giving estimates of the diffusivities in the axial and radial directions, D_A and D_R, with respect to the cylindrical symmetry axis of the crystallites. The observations $D_R >> D_A$ and $D_A \approx 0$ are consistent with diffusion in a lamellar liquid crystal with planar surfactant bilayers being nearly impermeable to water (Callaghan and Söderman, 1983). For the isotropic restriction phantom Figure 3(c), the signal depends strongly on ω_cent as expected. In this case there is no clear

190 stratification of data points into separate master curves on account of the interplay between b_Δ and ω_cent as reported in the legend in Figure 3(a) and explained in detail below Eq. (32). The minor dependence of ω_cent on b_Δ is admittedly a drawback of our current approach for generating waveforms, which we however believe is justified by the simplicity and transparency of the mathematical expressions in Eqs. (24)-(32). Combined with an isotropic Gaussian component, the diffusion spectrum $D(\omega)$ for spherical restriction in Eq. (18) yields an excellent fit to the acquired data, showing that the data features no dependence

195 on the value of b_Δ. The obtained diffusivities are consistent with previous results for extra- and intracellular water in yeast cell sediments (Åslund and Topgaard, 2009). Taken together, the data in Figure 3 verifies that the set of waveforms allow detailed exploration of the 2D $\omega_\text{cent},b_\Delta$-plane of multidimensional diffusion encoding.
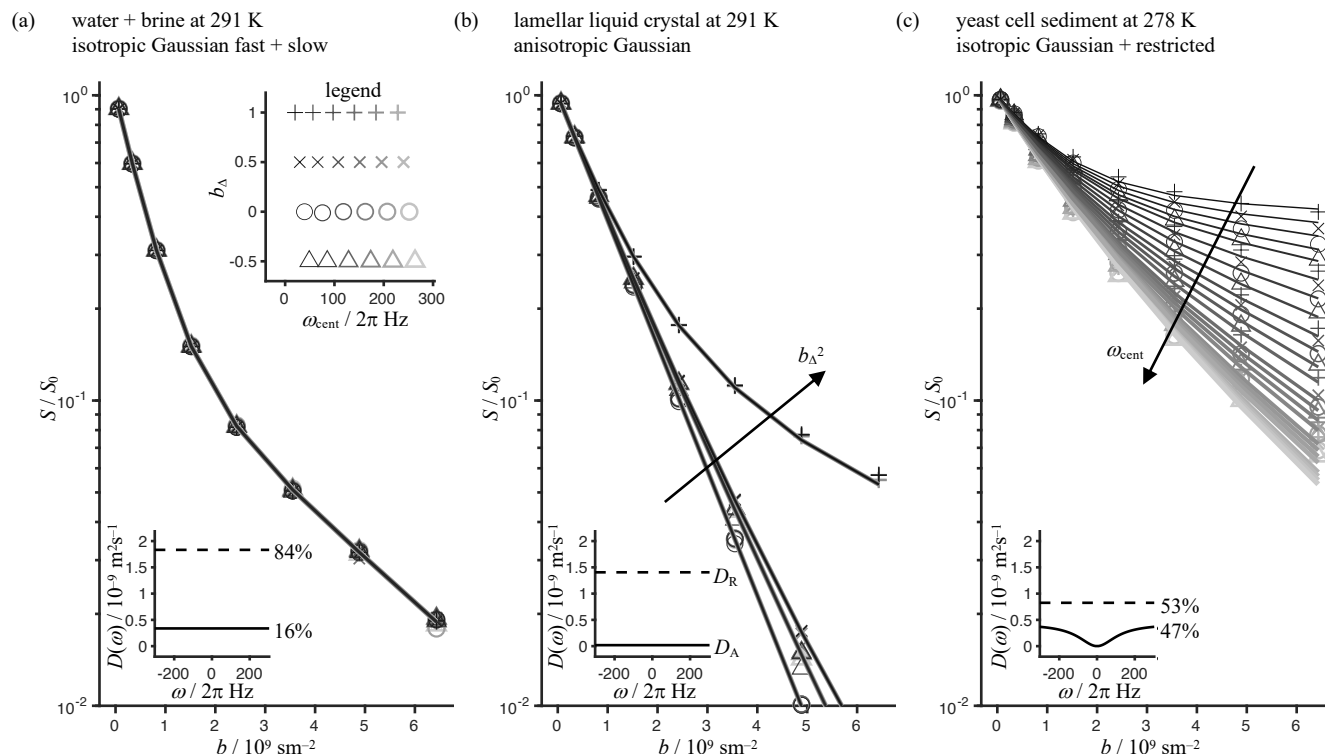
Figure 3. Experimental (markers) and fitted (lines) normalized powder-averaged signal S/S_0 vs. b-value for phantoms with well-defined diffusion properties. (**a**) Tube-in-tube assembly of pure water and a concentrated solution of magnesium nitrate in water ("brine") giving rise to two isotropic Gaussian (ω-independent) components. Two-component fit based on Eq. (11) gives diffusion spectra $D(\omega)$ as shown in the inset with percentages indicating the relative contributions. The legend shows the 24 investigated values in the ω_cent (gray scale) and b_Δ (marker style) space corresponding to the gradient waveforms in Figure 2 with duration $\tau = 25$ ms, maximum gradient strength 3 Tm^{-1}, and pairs of waveforms bracketing the 180° pulse in the spin-echo preparation. (**b**) Polydomain lamellar liquid crystal giving Gaussian axial and radial diffusivities, D_A and D_R, as estimated by a fit of Eq. (14). (**c**) Sediment of yeast cells with intra- and extracellular compartments, the former exhibiting restricted (ω-dependent) diffusion. The inset shows $D(\omega)$ resulting from a two-component fit with one Gaussian (dashed) and one spherically restricted (solid) component. For the latter component, the signal was obtained by numerical integration of Eq. (13) with $D(\omega)$ given by Eq. (18).

5   Conclusions and outlook

The proposed family of double-rotation gradient waveforms enables comprehensive sampling of both the frequency and "shape" dimensions of diffusion encoding as required for detailed characterization of restrictions and anisotropy in heterogeneous materials such as brain tissues. The present waveforms, deriving from simple geometrical considerations and generated by compact mathematical expressions, are suitable for pre-clinical investigations of tissue samples or small animals on high-gradient systems. By numerical optimizations to maximize the b-value for given gradient strength (Topgaard, 2013; Sjölund et al., 2015), mitigating image artifacts from eddy currents (Yang and McNab, 2019) and concomitant gradients (Szczepankiewicz et al., 2019), and further minimizing side-lobes in the encoding spectra (Hennel et al., 2020), we anticipate that the waveforms may be adapted for human *in vivo* studies. The merging of oscillating gradients (Aggarwal, 2020) and tensor-valued encoding (Reymbaut, 2020) into a common acquisition protocol encourages further development of a joint analysis framework, for instance by augmenting current nonparametric diffusion tensor distributions (Topgaard, 2019a) with a Lorentzian frequency dimension (Narvaez et al., 2021; Narvaez et al., 2022) or building on the concept of confinement tensors (Yolcu et al., 2016; Boito et al., 2022).

MAGNETIC RESONANCE
Discussions

Author contributions

DT conceived the project. HJ, LS, and DT developed theory and software. HJ acquired data. HJ and DT processed and analyzed data. HJ, LS, and DT wrote the manuscript.

References

Aggarwal, M.: Restricted diffusion and spectral content of the gradient waveforms, In: Topgaard, D. (Ed.), Advanced Diffusion Encoding Methods in MRI, Royal Society of Chemistry, Cambridge, UK, pp. 103-122, doi: 10.1039/9781788019910-00103, 2020.

Andrew, E. R., Bradbury, A., Eades, R. G.: Removal of dipolar broadening of nuclear magnetic resonance spectra of solids by specimen rotation, Nature, 183, 1802-1803, doi: 10.1038/1831802a0, 1959.

Arbabi, A., Kai, J., Khan, A. R., Baron, C. A.: Diffusion dispersion imaging: Mapping oscillating gradient spin-echo frequency dependence in the human brain, Magn Reson Med, 83, 2197-2208, doi: 10.1002/mrm.28083, 2020.

Åslund, I., Topgaard, D.: Determination of the self-diffusion coefficient of intracellular water using PGSE NMR with variable gradient pulse length, J. Magn. Reson., 201, 250-254, doi: 10.1016/j.jmr.2009.09.006, 2009.

Basser, P. J., Mattiello, J., Le Bihan, D.: Estimation of the effective self-diffusion *tensor* from the NMR spin echo, J. Magn. Reson. B, 103, 247-254, doi: 10.1006/jmrb.1994.1037, 1994.

Boito, D., Yolcu, C., Özarslan, E.: Multidimensional diffusion MRI methods with confined subdomains, Front. Phys., 10, 830274, doi: 10.3389/fphy.2022.830274, 2022.

Boss, B. D., Stejskal, E. O.: Anisotropic diffusion in hydrated vermiculite, J. Chem. Phys., 43, 1068-1069, doi: 10.1063/1.1696823, 1965.

Callaghan, P. T.: Translational dynamics & magnetic resonance. Oxford University Press, Oxford, 2011.

Callaghan, P. T., Manz, B.: Velocity exchange spectroscopy, J. Magn. Reson. A, 106, 260-265, doi: 10.1006/jmra.1994.1036, 1994.

Callaghan, P. T., Söderman, O.: Examination of the lamellar phase of Aerosol OT/water using pulsed field gradient nuclear magnetic resonance, J. Phys. Chem., 87, 1737-1744, doi: 10.1021/j100233a019, 1983.

Caprihan, A., Fukushima, E.: Flow measurements by NMR, Phys. Rep., 198, 195-235, doi: 10.1016/0370-1573(90)90046-5, 1990.

Carr, H. Y., Purcell, E. M.: Effects of diffusion on free precession in nuclear magnetic resonance experiments, Phys. Rev., 94, 630-638, doi: 10.1103/PhysRev.94.630, 1954.

Cory, D. G., Garroway, A. N., Miller, J. B.: Applications of spin transport as a probe of local geometry, Polymer Prepr., 31, 149-150, doi: 1990.

Daimiel Naranjo, I., Reymbaut, A., Brynolfsson, P., Lo Gullo, R., Bryskhe, K., Topgaard, D., Giri, D. D., Reiner, J. S., Thakur, S., Pinker-Domenig, K.: Multidimensional diffusion magnetic resonance imaging for characterization of tissue microstructure in breast cancer patients: A prospective pilot study, Cancers, 13, 1606, doi: 10.3390/cancers13071606, 2021.

de Almeida Martins, J. P., Topgaard, D.: Two-dimensional correlation of isotropic and directional diffusion using NMR, Phys. Rev. Lett., 116, 087601, doi: 10.1103/PhysRevLett.116.087601, 2016.

Douglass, D. C., McCall, D. W.: Diffusion in paraffin hydrocarbons, J. Phys. Chem., 62, 1102-1107, doi: 10.1021/j150567a020, 1958.

Eriksson, S., Lasič, S., Nilsson, M., Westin, C.-F., Topgaard, D.: NMR diffusion encoding with axial symmetry and variable anisotropy: Distinguishing between prolate and oblate microscopic diffusion tensors with unknown orientation distribution, J. Chem. Phys., 142, 104201, doi: 10.1063/1.4913502, 2015.

265   Eriksson, S., Lasič, S., Topgaard, D.: Isotropic diffusion weighting by magic-angle spinning of the q-vector in PGSE NMR, J. Magn. Reson., 226, 13-18, doi: 10.1016/j.jmr.2012.10.015, 2013.

Frydman, L., Chingas, G. C., Lee, Y. K., Grandinetti, P. J., Eastman, M. A., Barrall, G. A., Pines, A.: Variable-angle correlation spectroscopy in solid-state nuclear magnetic resonance, J. Chem. Phys., 97, 4800-4808, doi: 10.1063/1.463860, 1992.

Haeberlen, U.: High resolution NMR in solids. Selective averaging. Academic Press, New York, 1976.

270   Hahn, E. L.: Spin echoes, Phys. Rev., 80, 580-594, doi: 10.1103/PhysRev.80.580, 1950.

Hennel, F., Michael, E. S., Pruessmann, K. P.: Improved gradient waveforms for oscillating gradient spin-echo (OGSE) diffusion tensor imaging, NMR Biomed, e4434, doi: 10.1002/nbm.4434, 2020.

Kärger, J.: Zur Bestimmung der Diffusion in einem Zweibereichsystem mit Hilfe von gepulsten Feldgradienten, Ann. Phys., 479, 1-4, doi: 10.1002/andp.19694790102, 1969.

275   Kindlmann, G.: Superquadric tensor glyphs, In: Deussen, O., Hansen, C., Keim, D.A., Saupe, D. (Eds.), Proceedings IEEE TVCG/EG Symposium on Visualization, Eurographics Association Aire-la-Ville, Switzerland, pp. 147-154, doi: 10.2312/VisSym/VisSym04/147-154, 2004.

Kingsley, P. B.: Introduction to diffusion tensor imaging mathematics: Part II. Anisotropy, diffusion-weighting factors, and gradient encoding schemes, Conc. Magn. Reson. A, 28A, 123-154, doi: 10.1002/cmr.a.20049, 2006.

280   Lasič, S., Szczepankiewicz, F., Eriksson, S., Nilsson, M., Topgaard, D.: Microanisotropy imaging: quantification of microscopic diffusion anisotropy and orientational order parameter by diffusion MRI with magic-angle spinning of the q-vector, Front. Physics, 2, 11, doi: 10.3389/fphy.2014.00011, 2014.

Le Bihan, D., Breton, E., Lallemand, D., Grenier, P., Cabanis, E., Laval-Jeantet, M.: MR imaging of intravoxel incoherent motions - application to diffusion and perfusion in neurological disorders, Radiology, 161, 401-407, doi:

285   10.1148/radiology.161.2.3763909, 1986.

Lundell, H., Lasič, S.: Diffusion encoding with general gradient waveforms, In: Topgaard, D. (Ed.), Advanced Diffusion Encoding Methods in MRI, Royal Society of Chemistry, Cambridge, UK, pp. 12-67, doi: 10.1039/9781788019910-00012, 2020.

Lundell, H., Nilsson, M., Dyrby, T. B., Parker, G. J. M., Cristinacce, P. L. H., Zhou, F. L., Topgaard, D., Lasič, S.:

290   Multidimensional diffusion MRI with spectrally modulated gradients reveals unprecedented microstructural detail, Sci. Rep., 9, 9026, doi: 10.1038/s41598-019-45235-7, 2019.

Lundell, H., Sønderby, C. K., Dyrby, T. B.: Diffusion weighted imaging with circularly polarized oscillating gradients, Magn. Reson. Med., 73, 1171-1176, doi: 10.1002/mrm.25211, 2015.

Malmborg, C., Sjöbeck, M., Brockstedt, S., Englund, E., Söderman, O., Topgaard, D.: Mapping the intracellular fraction of

295   water by varying the gradient pulse length in q-space diffusion MRI, J. Magn. Reson., 180, 280-285, doi: 10.1016/j.jmr.2006.03.005, 2006.

Mills, R.: Self-diffusion in normal and heavy water in the range 1-45°, J. Phys. Chem., 77, 685-688, doi: 10.1021/j100624a025, 1973.

Mori, S., van Zijl, P. C. M.: Diffusion weighting by the trace of the diffusion tensor within a single scan, Magn. Reson. Med.,

300   33, 41-52, doi: 10.1002/mrm.1910330107, 1995.

Narvaez, O., Svenningsson, L., Yon, M., Sierra, A., Topgaard, D.: Massively multidimensional diffusion-relaxation correlation MRI, Front. Phys., 9, 793966, doi: 10.3389/fphy.2021.793966, 2022.

Narvaez, O., Yon, M., Jiang, H., Bernin, D., Forssell-Aronsson, E., Sierra, A., Topgaard, D.: Model-free approach to the interpretation of restricted and anisotropic self-diffusion in magnetic resonance of biological tissues, arXiv:2111.07827, doi:

305   10.48550/arXiv.2111.07827, 2021.

Nielsen, J. S., Dyrby, T. B., Lundell, H.: Magnetic resonance temporal diffusion tensor spectroscopy of disordered anisotropic tissue, Sci. Rep., 8, 2930, doi: 10.1038/s41598-018-19475-y, 2018.

Nilsson, M., Szczepankiewicz, F., Lampinen, B., Ahlgren, A., de Almeida Martins, J. P., Lasič, S., Westin, C.-F., Topgaard, D.: An open-source framework for analysis of multidimensional diffusion MRI data implemented in MATLAB, Proc. Intl.

310   Soc. Mag. Reson. Med., 26, 5355, doi: 2018.

Parsons, E. C., Does, M. D., Gore, J. C.: Modified oscillating gradient pulses for direct sampling of the diffusion spectrum suitable for imaging sequences, Magn. Reson. Imaging, 21, 279-285, doi: 10.1016/s0730-725x(03)00155-3, 2003.

Persson, N.-O., Fontell, K., Lindman, B., Tiddy, G. J. T.: Mesophase structure studies by deuteron magnetic resonance observations for the sodium octanoate-decanol-water system, J. Colloid Interface Sci., 53, 461-466, doi: 10.1016/0021-315   9797(75)90063-6, 1975.

Price, W. S.: NMR studies of translational motion. Cambridge University Press, Cambridge, 2009.

Reymbaut, A.: Diffusion anisotropy and tensor-valued encoding, In: Topgaard, D. (Ed.), Advanced Diffusion Encoding Methods in MRI, Royal Society of Chemistry, Cambridge, UK, pp. 68-102, doi: 10.1039/9781788019910-00068, 2020.

Reymbaut, A., Zheng, Y., Li, S., Sun, W., Xu, H., Daimiel Naranjo, I., Thakur, S., Pinker-Domenig, K., Rajan, S., Vanugopal, 320   V. K., Mahajan, V., Mahajan, H., Critchley, J., Durighel, G., Sughrue, M., Bryskhe, K., Topgaard, D.: Clinical research with advanced diffusion encoding methods in MRI, In: Topgaard, D. (Ed.), Advanced Diffusion Encoding Methods in MRI, Royal Society of Chemistry, Cambridge, UK, pp. 406-429, doi: 10.1039/9781788019910-00406, 2020.

Samoson, A., Lippmaa, E., Pines, A.: High resolution solid-state NMR: Averaging of second-order effects by means of a double-rotor, Mol. Phys., 65, 1013-1018, doi: 10.1080/00268978800101571, 1998.

325   Sjölund, J., Szczepankiewicz, F., Nilsson, M., Topgaard, D., Westin, C.-F., Knutsson, H.: Constrained optimization of gradient waveforms for generalized diffusion encoding, J. Magn. Reson., 261, 157-168, doi: 10.1016/j.jmr.2015.10.012, 2015.

Stejskal, E. O., Tanner, J. E.: Spin diffusion measurements: Spin echoes in the presence of a time-dependent field gradient, J. Chem. Phys., 42, 288-292, doi: 10.1063/1.1695690, 1965.

Stepišnik, J.: Analysis of NMR self-diffusion measurements by a density matrix calculation, Physica B, 104, 305-364, doi: 330   10.1016/0378-4363(81)90182-0, 1981.

Stepišnik, J.: Time-dependent self-diffusion by NMR spin-echo, Physica B, 183, 343-350, doi: 10.1016/0921-4526(93)90124-O, 1993.

Stepišnik, J., Callaghan, P. T.: The long time tail of molecular velocity correlation in a confined fluid: observation by modulated gradient spin-echo NMR, Physica B, 292, 296-301, doi: 10.1016/S0921-4526(00)00469-5, 2000.

335   Szczepankiewicz, F., Westin, C. F., Nilsson, M.: Maxwell-compensated design of asymmetric gradient waveforms for tensor-valued diffusion encoding, Magn. Reson. Med., 82, 1424-1437, doi: 10.1002/mrm.27828, 2019.

Tanner, J. E.: Self diffusion of water in frog muscle, Biophys. J., 28, 107-116, doi: 10.1016/S0006-3495(79)85162-0, 1979.

Topgaard, D.: Isotropic diffusion weighting in PGSE NMR: Numerical optimization of the q-MAS PGSE sequence, Microporous Mesoporous Mater., 178, 60-63, doi: 10.1016/j.micromeso.2013.03.009, 2013.

340   Topgaard, D.: Director orientations in lyotropic liquid crystals: Diffusion MRI mapping of the Saupe order tensor, Phys. Chem. Chem. Phys., 18, 8545-8553, doi: 10.1039/c5cp07251d, 2016.

Topgaard, D.: Multidimensional diffusion MRI, J. Magn. Reson., 275, 98-113, doi: 10.1016/j.jmr.2016.12.007, 2017.

Topgaard, D.: Diffusion tensor distribution imaging, NMR Biomed., 32, e4066, doi: 10.1002/nbm.4066, 2019a.

Topgaard, D.: Multiple dimensions for random walks, J. Magn. Reson., 306, 150-154, doi: 10.1016/j.jmr.2019.07.024, 2019b.

345   Wadsö, L., Anderberg, A., Åslund, I., Söderman, O.: An improved method to validate the relative humidity generation in sorption balances, Eur. J. Pharm. Biopharm., 72, 99-104, doi: 10.1016/j.ejpb.2008.10.013, 2009.

Woessner, D. E.: N.M.R. spin-echo self-diffusion measurements on fluids undergoing restricted diffusion, J. Phys. Chem., 67, 1365-1367, doi: 10.1021/j100800a509, 1963.

Xu, J., Jiang, X., Devan, S. P., Arlinghaus, L. R., McKinley, E. T., Xie, J., Zu, Z., Wang, Q., Chakravarthy, A. B., Wang, Y., 350   Gore, J. C.: MRI-cytometry: Mapping nonparametric cell size distributions using diffusion MRI, Magn. Reson. Med., 85, 748-761, doi: 10.1002/mrm.28454, 2021.

Yang, G., McNab, J. A.: Eddy current nulled constrained optimization of isotropic diffusion encoding gradient waveforms, Magn. Reson. Med., 81, 1818-1832, doi: 10.1002/mrm.27539, 2019.

Yolcu, C., Memic, M., Simsek, K., Westin, C. F., Özarslan, E.: NMR signal for particles diffusing under potentials: From path 355   integrals and numerical methods to a model of diffusion anisotropy, Phys. Rev. E, 93, 052602, doi: 10.1103/PhysRevE.93.052602, 2016.